Dalton Transactions

ROYAL SOCIETY OF CHEMISTRY

PAPER

View Article Online
View Journal | View Issue

Cite this: *Dalton Trans.*, 2025, **54**, 2860

Synthesis and characterization of heptacoordinated molybdenum(II) complexes supported with 2,6-bis(pyrazol-3-yl)pyridine (bpp) ligands†

Arno Estival,[a] Luis E. Blancarte,[b] Loïc Pinto,[a] Romane Pointis,[a] Nathan Galas,[a] Alix Sournia-Saquet,[a] Laure Vendier,[a] Rosa Santillan,[c] Norberto Farfán,[b] Jean-Baptiste Sortais,[a] Mary Grellier[a] and Antoine Simonneau *[a]

Functional pincer ligands that engage in metal–ligand cooperativity and/or are capable of redox non-innocence have found a great deal of success in catalysis. These two properties may be found in metal complexes of the 2,6-bis(pyrazol-3-yl)pyridine (bpp) ligands. With this goal in mind, we have attempted the coordination of 2,6-bis(5-trifluoromethylpyrazol-3-yl)pyridine (L^{CF3}) and its ^{t}Bu analogue 2,6-bis(5-*tert*-butylpyrazol-3-yl)pyridine (L^{tBu}) to Mo(0) by reactions with mixed phosphine/carbonyl complexes $[Mo(CO)_2(MeCN)_{n-1}(PMe_{3-n}Ph_n)_{5-n}]$ **1–3** ($1 \leq n \leq 3$). These afforded mixtures of several Mo compounds among which low yields of heptacoordinated Mo(II) complexes $[Mo(CO)_2(bpp)(PMe_{3-n}Ph_n)_2]$ **4a–c** (L^{CF3}-supported) and **5a–c** (L^{tBu}-supported) bearing a doubly deprotonated bpp ligand were systematically produced. More selective syntheses of **4a–c** and **5a–c** were achieved by repeating these experiments in the presence of an oxidant (AgOAc or Ag_2O), with moderate to good yields. **4a–c** and **5a–c** were characterized by means of NMR, IR and UV-Vis spectroscopies, sc-XRD and cyclic and square-wave voltammetries for **4a**, **4b** and **5b**. The deprotonated L^{tBu} ligand in **5a–c** is re-protonated with 2 equiv. of HOTf to afford the dicationic $[Mo(CO)_2(L^{tBu})(PMe_{3-n}Ph_n)_2][OTf]_2$ complexes **6a–c**. Acidic treatment of **4a–c** led to the decomposition of the complexes.

Received 21st November 2024,
Accepted 4th January 2025

DOI: 10.1039/d4dt03264k

rsc.li/dalton

Introduction

Tridentate ligands that enforce meridional coordination fall under the generic denomination of "pincer" ligands. By providing access to well-defined and easily tunable coordination spheres, pincer ligands have found widespread use in various fields of catalysis and inorganic and organometallic chemistry.[1–6] By introduction of functions on the pincer ligand that may participate in metal–ligand cooperativity and/or offer the possibility to store electrons to grant it (photo)redox non-innocence, chemists are able to design pincer-supported metal complexes with specifically engineered reactivity.[7–13] The introduction of nitrogenous groups or heterocycles remains a prominent strategy to provide either property, sometimes both. As an example, the bis(pyrazol-3-yl)pyridine (bpp) ligand family[14] allows, thanks to its pyrazolyl arms, embedding of proton-responsive sites, while the conjugation of the three N-heterocycles provides a low-energy LUMO suited for electron storage or charge transfer. Substituents may easily be introduced on N1 or C5 of the pyrazoles to modulate the properties of the ligand. Historically, bpp ligands were first employed for the design of Fe-based spin-crossover (SCO) complexes and materials, and Fe(bpp) compounds continue to actively nurture this field of research.[15–20] Nowadays, the bpp platform has been associated with many elements of the p, d and f blocks to provide complexes with a vast range of applications: luminescence,[21–27] imaging,[28] liquid–liquid extraction,[29,30] medicinal chemistry,[31–33] small molecule activation[34–42] and catalysis.[43–48] In the past few years, our group has been interested in the use of phosphine-supported molybdenum and tungsten complexes for small molecule activation.[49–57] While phosphines remain generally spectator ligands, proton-responsiveness and redox non-innocence are two properties that are

[a]*LCC-CNRS, Université de Toulouse, CNRS, UPS, 205 route de Narbonne, BP44099 F-31077 Toulouse cedex 4, France. E-mail: antoine.simonneau@lcc-toulouse.fr*
[b]*Facultad de Química, Departamento de Química Orgánica, Universidad Nacional Autónoma de México, 04510 CDMX, Mexico*
[c]*Departamento de Química, Centro de Investigación y de Estudios Avanzados del IPN, México D.F. Apdo. Postal 14–740, 07000, Mexico*

†Electronic supplementary information (ESI) available: A .pdf file compiling NMR, infrared and UV-Vis spectra, cyclic and square wave voltammograms, and crystallographic details. CCDC 2403147–2403152. For ESI and crystallographic data in CIF or other electronic format see DOI: https://doi.org/10.1039/d4dt03264k

desirable for this field of research. Because the bpp platform potentially offers both, we have attempted its pairing with molybdenum, a metal curiously absent from the catalogue of the already-reported, bpp-supported complexes,[58] fueled by the recent successes of Mo-pincer complexes in catalysis.[59–69] In this article, we show that our initial goal of coordinating different bpp ligands to Mo(0) ended in failure, presumably because the bpp platform is not suited for this oxidation state when other electron-donating ligands are present, promoting uncontrolled redox chemistry that leads to non-selective reaction outcomes. However, variable amounts of bpp/phosphine-supported, hepta-coordinated Mo(II) complexes in which the bpp ligand is deprotonated could be collected. By adjusting the reaction conditions, we were able to isolate and characterize in good to high yields a series of these compounds, the first Mo complexes incorporating the bpp platform (Fig. 1). All were characterized by multi-nuclei NMR spectroscopy, IR and UV/Vis spectrophotometry, single crystal X-ray diffraction (sc-XRD) and cyclic voltammetry (CV). The proton-responsiveness of the deprotonated bpp ligand in these edifices is demonstrated.

Results and discussion

Inspired by a recent body of work on pincer-supported molybdenum catalysts from the Beller group,[63–65,67,70] we attempted the coordination of the bpp platform to the family of heteroleptic Mo(0) complexes $[Mo(CO)_2(MeCN)_{n-1}(PMe_{3-n}Ph_n)_{5-n}]$ **1–3** ($1 \leq n \leq 3$).[71–74] We selected two different bpp ligands bearing either CF_3 ($\mathbf{L^{CF3}}$) or ^{t}Bu ($\mathbf{L^{tBu}}$) groups at their C5 positions and exerting opposite electronic effects on the platform. Attempts at coordinating either $\mathbf{L^{tBu}}$ or $\mathbf{L^{CF3}}$ to **1–3** under various conditions (refluxing toluene, 3–24 h) led to surprisingly unselective reaction mixtures, particularly messy in the $\mathbf{L^{tBu}}$ complexation experiments. From the reaction of **2** with $\mathbf{L^{CF3}}$, we could isolate the major diamagnetic compound **4b** from the reaction mixture (refluxing toluene, 3 h) bearing two $PMePh_2$ ligands ($^{31}P\{^1H\}$ NMR δ = 22.6 ppm, ^{19}F NMR δ = −61.5 ppm) and retaining two carbonyl ligands (ν_{sym} = 1880 cm^{-1} and ν_{asym} = 1948 cm^{-1}) in low yield (35%). Slow diffusion of hexane into a concentrated toluene solution allowed us to grow crystals suitable for single-crystal X-ray diffraction (sc-XRD) analysis. The molecular structure of **4b** is shown in Fig. 2, showing a C_2-symmetric, heptacoordinated molybdenum complex in which $\mathbf{L^{CF3}}$ is fully complexed to the Mo center. The C_2 axis spreads along the Mo–N_{py} bond (py = pyridine), and in the equatorial plane are found the phosphines, in trans relationship to each other, and the two N_{pz} atoms (pz = pyrazole). The carbonyl ligands complete the 7-coordination environment in an overall capped trigonal prismatic (CTP) geometry, occupying the edges as predicted for π-accepting ligands by molecular orbital analysis.[75] Attempts to localize protons on the unbound nitrogen atoms of the pyrazole arms in the Fourier density map were unsuccessful, while their positioning generated negative electron density in their environment. This coupled with the fact that a 7-coordinated Mo(0) compound would have 20 valence electrons as well as the absence of detectable N_{pz}–H proton resonances in the ^{1}H NMR spectrum convinced us we isolated a Mo(II) compound supported by a deprotonated $\mathbf{L^{CF3}}$ ligand. Diamagnetism dismisses the non-innocent character of the ligand in this complex. We were unable to identify the other product of these reactions, but the isolation of **4b** made us postulate that uncontrolled electron transfers may take place and that the redox active bpp platform[76,77] was perhaps not suited to stabilize molybdenum in oxidation state 0. We therefore wondered whether it would be possible to obtain **4b** selectively from **2** by adding two equivalents of a one electron oxidant. Indeed, in THF and in the presence of AgOAc, **4b** was isolated as a red crystalline solid from the reaction mixture in a much higher yield (69%, see Scheme 1). Repeating the experiment with precursors **1** or **3** allowed us to prepare compounds **4a** and **4c**, respectively, isolated as red powders (Scheme 1). Unfortunately, these conditions were not optimal when attempting complexation of $\mathbf{L^{tBu}}$, as comparatively lower yields of the **5a–c** congeners were recorded due to the formation of unidentified side-products. Reasoning that the acetate anion was probably assisting deprotonation of the $\mathbf{L^{CF3}}$ ligand in the reactions affording **4a–c**, we evaluated silver(I) oxide (Ag_2O) as oxidant having a more basic anion we thought would be more suited to the expectedly higher pK_a of the $\mathbf{L^{tBu}}$ ligand. This approach led to a substantially cleaner outcome after a comparatively longer reaction time for **5a** and facilitated its isolation (51% yield), but no difference was observed for the synthesis of **5b** and **5c**, even when excess Ag_2O was engaged (44 and 51% yield, respectively). Crystals generating sc-XRD data of sufficient quality could be grown for compounds **4a–c** and **5b** from concentrated THF solutions layered with pentane. In the case of **5a**, and despite several crystallization attempts, only microcrystalline materials were obtained. For **5c**, tiny, non-monocrystalline platelets were systematically obtained, some of them diffracting in the XRD apparatus. This brought confirmation of the atomic connectivity but the data were not of sufficient quality to comment on the metrics (Fig. 2). Pertinent structural parameters for **4a–c** and **5b** are gathered in Table 1. Akin to **4a**, **4b** and **4c** and **5b** and **5c** all feature a capped trigonal prismatic geometry, with a C_2 axis along the Mo–N_{py} bond and bisecting the OC–Mo–CO angle. Distortions from ideality occurring in the lattice are flagrant in the case of **4c** and **5c** for which the respective $\mathbf{L^{CF3}}$ and $\mathbf{L^{tBu}}$ ligands

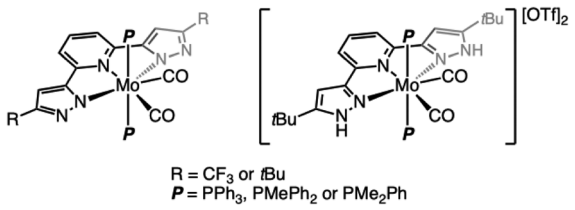

Fig. 1 Overview of the new heptacoordinated Mo(II) complexes described in this article.

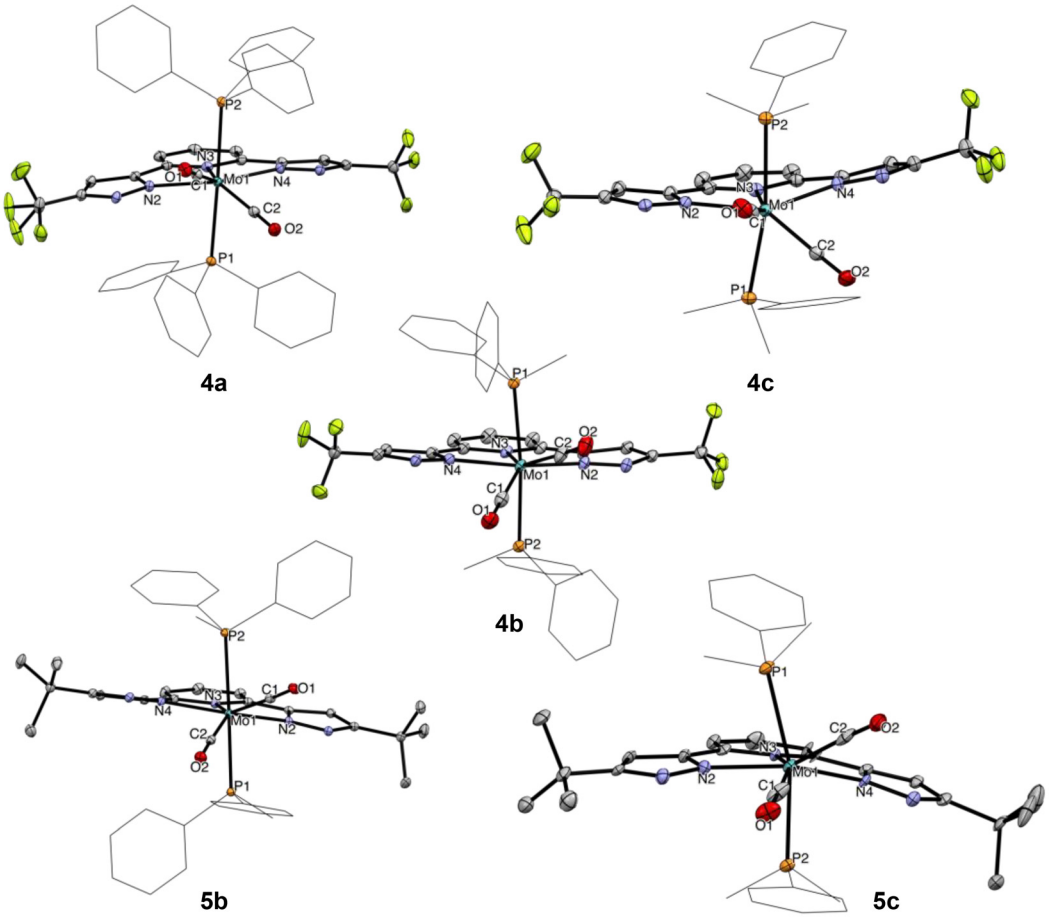

Fig. 2 Molecular structures of compounds **4a–c** and **5b** and **5c** in the solid state. Thermal ellipsoids at the 25% probability level. For clarity, hydrogen atoms are omitted and phosphorus substituents appear as wireframe. Two molecules are present in the asymmetric unit of the crystal of **5c** (*Z*′ = 2), and only one is represented. One of the CF_3 groups of **4a** presents a disorder.

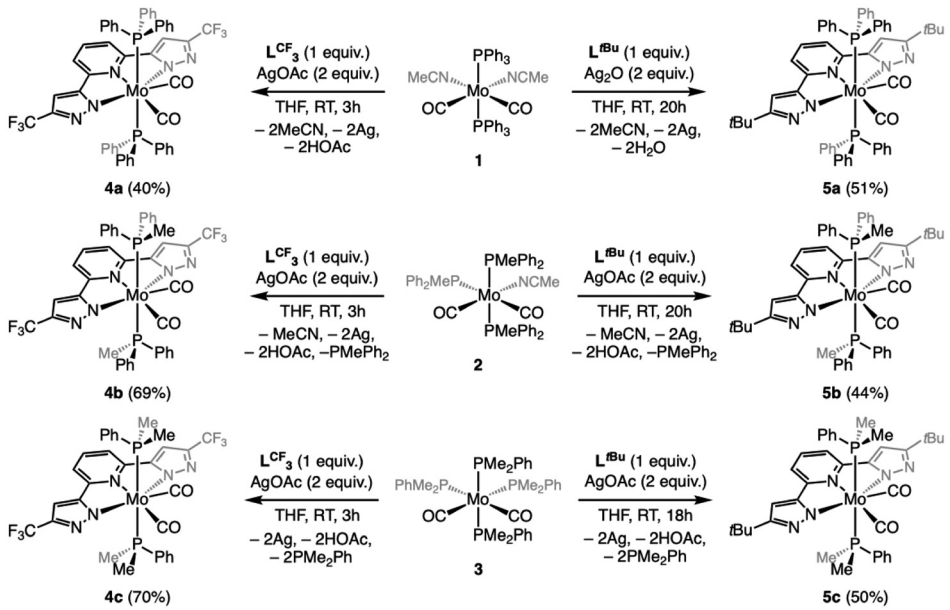

Scheme 1 Synthesis of the L^{CF3}-supported complexes **4a–c** and L^{tBu}-supported **5a–c**.

Table 1 Pertinent crystal data for **4a–c** and **5b** and **5c**

	4a	**4b**	**4c**	**5b**
Crystal system	Monoclinic	Monoclinic	Monoclinic	Orthorhombic
Space group	$P2_1/n$	$P2_1/n$	$P2_1/c$	$P\,b\,c\,a$
Mo–N2 (Å)	2.177(2)	2.171(2)	2.178(2)	2.173(1)
Mo–N3 (Å)	2.206(2)	2.200(2)	2.192(2)	2.190(1)
Mo–N4 (Å)	2.182(2)	2.162(2)	2.180(2)	2.168(1)
Mo–P1 (Å)	2.5711(6)	2.5131(8)	2.5540(7)	2.5218(7)
Mo–P2 (Å)	2.5442(6)	2.5226(8)	2.5190(7)	2.5372(7)
Mo–C1 (Å)	1.991(2)	1.974(3)	1.970(3)	1.963(2)
Mo–C2 (Å)	1.986(2)	1.979(3)	1.971(3)	1.980(2)
C1–O1 (Å)	1.137(3)	1.159(3)	1.144(4)	1.152(2)
C2–O2 (Å)	1.149(3)	1.168(4)	1.151(4)	1.147(2)

appear convex and the P–Mo–P array deviates significantly from linearity. In **5b**, the pyrazole arms are oppositely tilted away from the pyridine plane. All compounds of the $\mathbf{L^{CF3}}$ series crystallized in the monoclinic system, while **5b** and **5c** were found in the orthorhombic and triclinic ones, respectively. For the four complexes, the Mo atom is found at 2.16–2.18 Å from the nitrogen atoms of the pyrazol arms and 2.19–2.21 Å from the pyridine's N atom. No significant change is noticed when comparing the $\mathbf{L^{CF3}}$- and $\mathbf{L^{tBu}}$-supported complexes. For the $\mathbf{L^{CF3}}$ series, the shortest Mo–P bonds are found in **4b** ($PMePh_2$ ligand), a counter-intuitive observation since we would have expected the length of the Mo–P bonds would follow the trend of the phosphine's respective cone angles.[78] However, the Mo–CO bond lengths correlate rather well with the Tolman electronic parameter[78] (TEP) thereof, since a progressive shortening is observed as the TEP decreases (PPh_3 > $PMePh_2$ > PMe_2Ph), but the same is not true when considering the C–O bond lengths. Again, $PMePh_2$-supported **4b** stands out with the longest recorded C–O bonds.

Comparison of NMR spectroscopy data does not reveal any singular feature. The aromatic signals of the ligand in ^{1}H NMR are expectedly downfield shifted in the case of the $\mathbf{L^{CF3}}$ series. Of note, the bpp ligand exerts a limited influence on the chemical shift of the phosphorus resonances: 37.8 (**4a**) *vs.* 37.1 ppm (**5a**), 22.6 ppm for both **4b** and **5b**, and 9.6 (**4c**) *vs.* 11.1 ppm (**5c**).

Infrared spectroscopy analyses were performed on solid samples by the ATR method (Fig. S41–49†). Two symmetric and asymmetric C–O stretching bands are observed between 1950 and 1870 cm^{-1} (Table 2). Lower stretching frequencies were expectedly recorded for the $\mathbf{L^{tBu}}$ series, with differences of less than 10 wavenumbers from one series to the other. Only the symmetric C–O stretches follow the electronic parameter trend of the phosphine ligand. Electronic spectroscopy (Table 2, Fig. 3 and S50–S56†) did not allow detection of transitions in the visible region, even at high concentrations (10^{-3} M^{-1}). All complexes strongly absorb below 275 nm, which is not surprising given the conjugated aromatic nature of the bpp ligand and the presence of aromatic substituents on the phosphines, both permitting symmetry-allowed intraligand

Table 2 Pertinent spectroscopic parameters for **4a–c** and **5a–c**

	4a	**4b**	**4c**	**5a**	**5b**	**5c**
$\nu(CO)_{as}$ (cm^{-1})	1944	1948	1934	1938	1940	1946
$\nu(CO)_{sym}$ (cm^{-1})	1888	1880	1873	1886	1879	1877
λ_{abs} (nm) (ε [L mol^{-1} cm^{-1}])	252 (13 417)	247 (9969)	239 (12 007)	254 (19 584)	304 (3078)	304 (4606)
	291 (7019)	291 (4090)	291 (5010)		375 (2019)	373 (2844)
	324 (4492)	319 (3308)	317 (3470)			
	332 (3623)	359 (2588)	359 (2859)			
	362 (2221)					

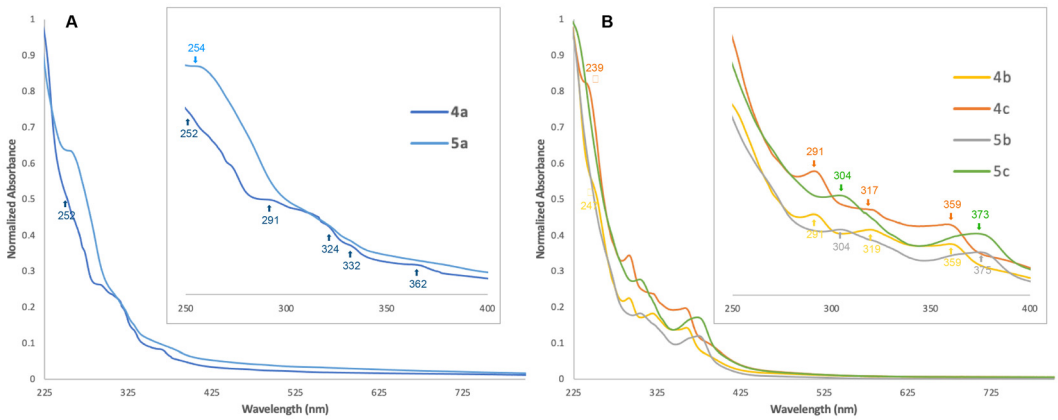

Fig. 3 Normalized UV-Vis spectra recorded at *ca.* 10^{-5} M^{-1} with magnification of the 250–400 nm region of (A) **4a** and **5a** and (B) **4b** and **4c** and **5b** and **5c**.

(IL) π–π* transition.[47] Shoulders are visible for **4a–c** and **5a** at 252, 247, 239 and 254 nm, respectively. The energetic cost of these transitions increases with the donating nature of the phosphine. In the $\mathbf{L^{CF3}}$ series, all complexes feature a less intense absorption at 291 nm, clearly visible for **4b** and **4c** but rather broad in the case of **4a**. Two other bands can be found in the recorded electronic spectra when moving towards near UV, difficult to discern in the case of PPh_3-supported **4a** and **5a**, but clearly visible for **4b** and **4c** and **5b** and **5c**. These two transitions are unchanging within a bpp series. The most blue-shifted ones have a higher energy cost in the case of the $\mathbf{L^{tBu}}$ series. Although trends can be extracted from the electronic spectra, the particular CTP geometry combined with the complexity of the ligand sphere makes it difficult for any tentative assignment of these transitions through a qualitative molecular orbital (MO) analysis, but few comments can be made. Bai *et al.* have shown in a computational study on the spectroscopic properties of homoleptic bis(2-pyridylpyrazolate)-supported square planar platinum(II) complexes[79] that the LUMO of the complexes is always a π* MO mainly localized on the pyridyl moiety, whatever electron-donating (*t*Bu) or -withdrawing (CF_3) group is carried by the pyrazolate arm. The absorptions with the largest molar absorptivity coefficient are mostly due to IL π → π* excitation, d → π* metal–ligand charge transfer (MLCT) or a mix thereof, in line with what is frequently observed for other pyridyl-azolate complexes,[80] while ligand field (LF) transitions occur in the far-UV. Given the similarities in the UV-Vis spectra within a bpp series (flagrant when comparing **4b** and **4c** or **5b** and **5c**, Fig. 3) it is probable that the observed bands are the results of bpp-centered π → π* IL transitions, or d → π^*_{bpp} MLCT ones, in line with the recorded molar absorption coefficients (>1000 L mol^{-1} cm^{-1}, Table 2). The d orbitals in a model C_{2v} CTP ML_7 complex (where L is σ-donating only) are all non-degenerate, with a set of two stabilized orbitals ($d_{x^2-y^2}$ and d_{yz}, both filled with an electron pair in the case of d^4 Mo(II)) and three destabilized ones (d_{xz}, d_{z^2}, and d_{xy}) (Fig. 4).[75] Both filled $d_{x^2-y^2}$ and d_{yz} orbitals overlap with π* (CO, bpp) or σ* (phosphines) orbitals located on the ligands, making various MLCT transitions possible. The d_{yz} orbital is oriented for overlap with the pyridyl component of a π^*_{bpp} orbital while being unperturbed by the phosphines. If IL and d_{yz} → π* transitions govern the near-UV part of the electronic spectrum of **4b** and **4c** and **5b** and **5c**, the phosphines should not exert a significant influence. Interestingly, the study by Bai *et al.* shows that the HOMO–LUMO gap grows larger when hydrogen is substituted by electron-withdrawing groups (–CF_3 or –C_3F_7) at the 3-position of the pyrazole ring, resulting in an overall blue-shift of the absorption. The trend is reversed when a *t*Bu group is present. In our case, considering the lowest energy absorption, **5b** and **5c** ($\mathbf{L^{tBu}}$-supported) exhibit transitions at 375 and 373 nm, respectively, red-shifted compared to the one of **4b** and **4c** ($\mathbf{L^{CF3}}$-supported, both 359 nm). We cannot exclude that other MLCT transitions such as d → π^*_{CO}[81] or d → σ^*_P[82–85] participate also in the overall spectrum.

The electrochemical behavior of complexes **4a**, **4b** and **5b** was examined in THF by cyclic and square wave voltammetries (Table 3, Fig. 5 and S63–84†), with tetra(*n*-butyl)ammonium hexafluorophosphate (TBA[PF_6]) as the supporting electrolyte. Towards cathodic potentials, voltammograms (Fig. 5, bottom left and S73 and S77†) reveal an irreversible reduction wave for **4b** and **5b** occurring at E_p = −1.63 V and −2.00 V *vs.* SCE, respectively, and two very close reductions at E_p = −1.67 and −1.83 V for **4a**. The free, protonated ligands $\mathbf{L^{CF3}}$ and $\mathbf{L^{tBu}}$ both exhibit an irreversible reduction wave under the same conditions at slightly lower potentials (E_p = −1.93 and −2.21 V *vs.* SCE, respectively, see Fig. S63–68†). The more cathodically shifted potential in the case of the *t*Bu-substituted compound (**5b**) is consistent with the inductive donor effects of the *t*Bu groups resisting reduction. Irreversibility could thus stem from a ligand-centered reduction that compromises the stability of the complexes, which is further corroborated by equal first reduction peak potentials for **4a** and **4b**, both supported by $\mathbf{L^{CF3}}$. While a ligand-centered reduction indicates its possible non-innocent character, its irreversible nature suggests that

Table 3 Pertinent potentials (V *vs.* SCE) for oxidation and reduction of **4a**, **4b** and **5b** determined by cyclic voltammetry

	Oxidation		Reduction	
	I	II	I	II
4a	0.97[b] (64[c])	1.27[a]	−1.67[a]	−1.83[a]
4b	0.92[b] (78[c])	1.19[a]	−1.63[a]	−2.36[a]
5b	0.56[b] (107[c])	0.94[b]	−2.00[a]	

[a] Irreversible waves, E_p. [b] Quasi-reversible waves, $E_{1/2}$. [c] Peak-to-peak separation, ΔE_p in mV.

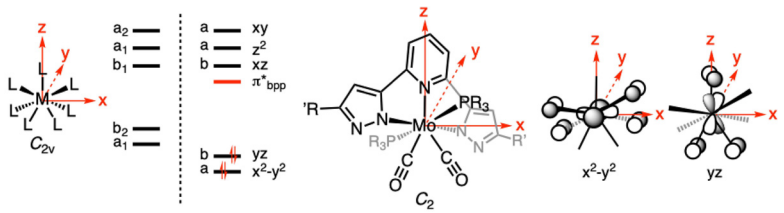

Fig. 4 d orbital splitting for a model C_{2v} ML_7 complex (left) and qualitative prediction of the frontier orbitals for the series of complexes **4a–c** and **5a–c** with depiction of possible overlap of filled d orbitals with ligands' π-shaped MOs.

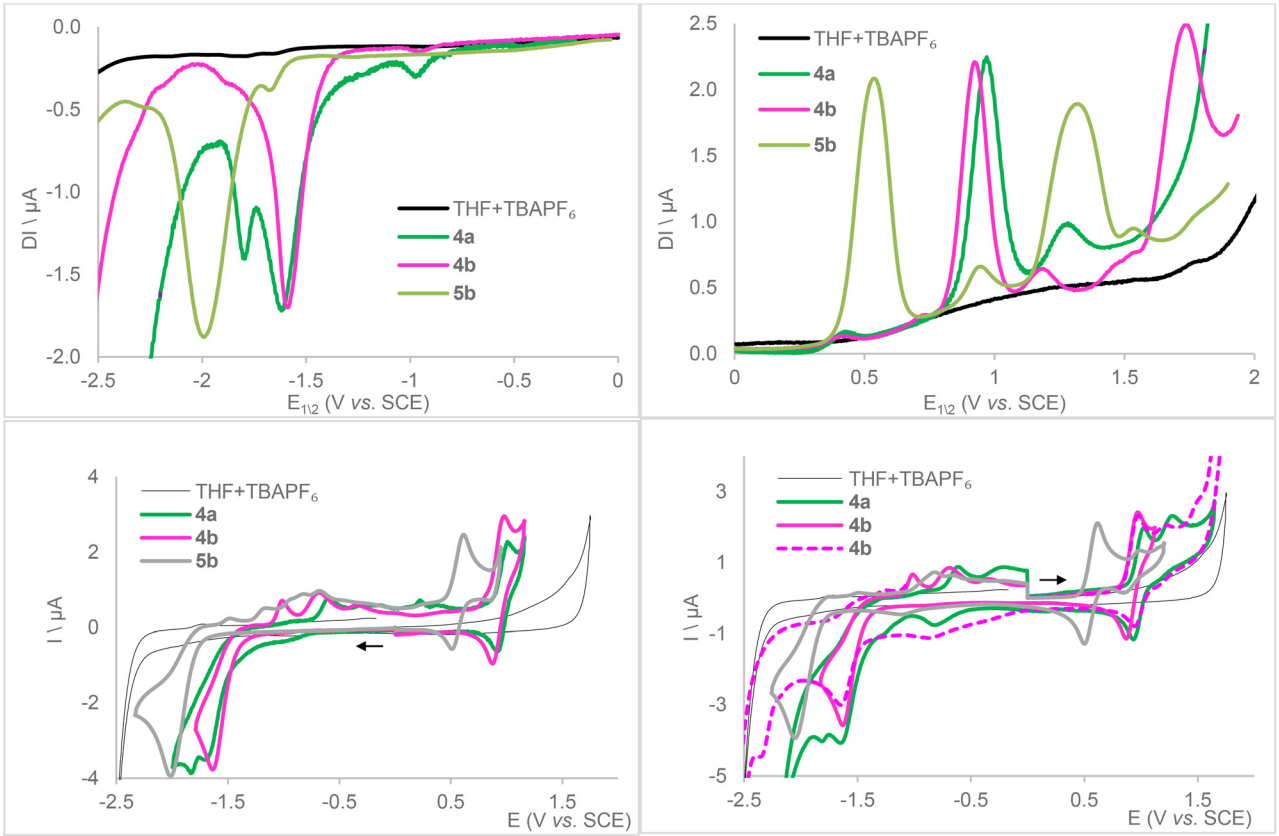

Fig. 5 Square wave (top) and cyclic voltammograms on a glassy carbon electrode for compounds **4a**, **4b** and **5b** ([C] = 1 mM) recorded under Ar in dry THF with 0.1 M TBA[PF_6] supporting electrolyte (cyclic voltammetry: scan rate 0.2 V s^{-1}; square wave voltammetry parameters: modulation amplitude 20 mV, frequency 20 Hz, and step potential 5 mV or 0.1 V s^{-1}).

practical application may be complicated. For both **4a** and **4b**, this event is followed by a second irreversible wave at E_p = −1.83 and −2.36 V, respectively. It is possible that the less σ-donating characteristic of PPh_3 grants access to an irreversible $Mo^{2+} \rightarrow Mo^{1+}$ reduction event in **4a** that is shifted cathodically for **4b** but, within the swept voltage range, out of reach for **5b** that features a more electron-rich ligand sphere. Upon return to anodic potentials, several oxidation waves between −1.5 and 0 V as well as an increase of capacitive current are noticed, suggesting the decomposition of the reduced complexes into several, unidentified species that may also adsorb on the working electrode. Beyond 0 V, CV curves of **4a**, **4b**, and **5b** show a quasi-reversible wave at $E_{1/2}$ = 0.97, 0.92, and 0.56 V *vs.* SCE, respectively, also observed when first scanning towards anodic potentials. This can reasonably be assigned to $Mo^{2+} \rightarrow Mo^{3+}$ oxidation (Fig. 5, bottom). Loss of reversibility is observed upon return of voltage sweeping from high potentials (Fig. 5, bottom right, **4b**). This is followed by a second, smaller peak at E_p = 1.27, 1.19 and 0.94 V *vs.* SCE, respectively, more or less reversible. Depending on the product, other irreversible oxidation waves may be observed. The various mechanisms have not been identified, but we can consider the following hypotheses which are plausible among others: CO or phosphine loss as their ligand properties become a poor match for high oxidation state Mo, ligand degradation, or fluoride abstraction from the supporting electrolyte by a now-electrophilic metal center.

Proton-responsiveness of the complexes was evaluated by treating solutions of **4a–c** and **5a–c** in THF with two equivalents of trific acid (HOTf) (Scheme 2).[46] In the case of the $\mathbf{L}^{CF3}$ series, intractable mixtures containing paramagnetic compounds as well as the free ligand were obtained. It is likely that protonation of the electron-poor bpp ligand substantially labilizes it, compromising the stability of the thus-generated species. Conversely, the $\mathbf{L}^{tBu}$-supported complexes **5a–c** were readily protonated to afford the dicationic products **6a–c** preci-

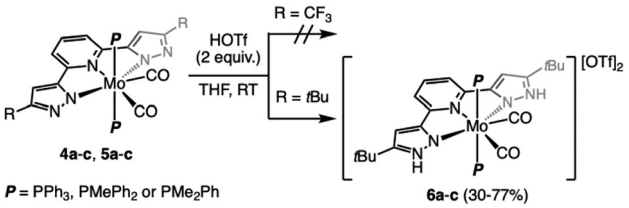

Scheme 2 Reactions of the heptacoordinated Mo complexes with HOTf.

pitating out of the reaction mixture as yellow solids in moderate (**5a**, **5c**) to good yields (**5b**). Product **6b** could be crystallized from acetonitrile, affording a material suitable for an sc-XRD study. The solid-state structure of **6b** is shown in Fig. 6. It crystallizes in the monoclinic crystal system and the $C2/c$ space group. A two-fold rotation axis spreads again along the Mo–N_{py} bond. Despite several attempts, a high-quality structure could not be obtained either for **6b** ($R_{int} > 0.12$) or for **6a** and **6c**. The presence of the protons on the pyrazole arms of **6b** could be ascertained from the Fourier difference map.

Compared to **5b**, **6b** features elongated Mo–CO bonds (2.030(11) *vs.* 1.972(2) on average for **5b**) and Mo–N_{pz} bonds (2.192(6) *vs.* 2.171(1) on average for **5b**), reflecting the overall diminished donating character of the pyrazole arms. This is counter-balanced by a shortened Mo–N_{py} bond (2.162(9) *vs.* 2.190(1) for **5b**). Other metrics are roughly similar. IR data point to a diminished back donation to the CO ligands, in line with the protonated $\mathbf{L}^{t\mathbf{Bu}}$ becoming less σ-donating and more π-accepting. Bands related to CO bond elongation are all hypsochromically shifted, more drastically for **6b** by comparison with **6a** and **6c** ($\Delta\nu_{as}$ = 15, 22 and 7 cm^{-1} and $\Delta\nu_{sym}$ = 14, 29 and 10 cm^{-1} for **6a–c**, respectively).

Cyclic voltammetry run on a solution of **6b** in THF with TBA[PF_6] as the electrolyte expectedly contrasted with that of **5b**, with the presence of acidic protons complicating the electrochemistry (Fig. 7 and S81–S84† for square wave voltammetry). Four irreversible reduction waves are observed at E_p = −0.63, −1.16, −1.59 and −1.96 V and an irreversible oxidation one at 1.45 V *vs.* SCE. The latter occurs at a higher potential than for neutral **5b** (reversible wave at 0.94 V) but matches its second oxidation wave. The fourth reduction wave occurs at a very close potential to the reduction wave recorded for **5b** (−2.00 V), so we assume this could be the result of regenerated **5b** within the electrochemical cell. A two-electron reduction would be sufficient to get **5b** from **6b** by evolution of H_2. However, three redox events are recorded before reaching the most cathodic one, two of them could reasonably be the result of sequential reductions of the acidic protons carried by the pyrazoles. Further investigations regarding the behavior of compounds **6a–c** are necessary to understand the fate thereof under reducing conditions.

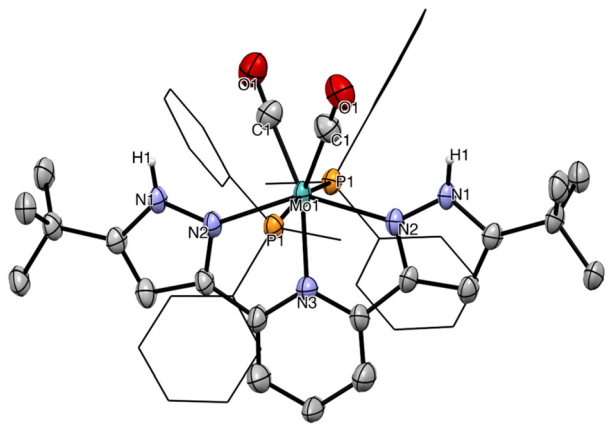

Fig. 6 Molecular structure of compound **6b** in the solid state. Thermal ellipsoids at the 25% probability level. For clarity, counterions and hydrogen atoms (except those bound to the N_{pz}) are omitted, and phosphorus substituents appear as wireframe.

Conclusions

In this article, we have attempted the coordination of tridentate, pincer-type 2,6-bis(pyrazol-3-yl)pyridine (bpp) ligands $\mathbf{L}^{\mathbf{CF3}}$ (bearing a CF_3 group at the C5 position of the pyrazole arm) and $\mathbf{L}^{t\mathbf{Bu}}$ (bearing instead a *t*Bu group) to molybdenum(0) precursors. With the chosen precursors [Mo$(CO)_2(MeCN)_{n-1}(PMe_{3-n}Ph_n)_{5-n}$] **1–3** ($1 \le n \le 3$), unclean reactions produced among other unidentified products heptacoordinated diamagnetic Mo(II) compounds [Mo$(CO)_2$(bpp)$(PMe_{3-n}Ph_n)_2$] **4a–c** ($\mathbf{L}^{\mathbf{CF3}}$-supported) and **5a–c** ($\mathbf{L}^{t\mathbf{Bu}}$-supported)

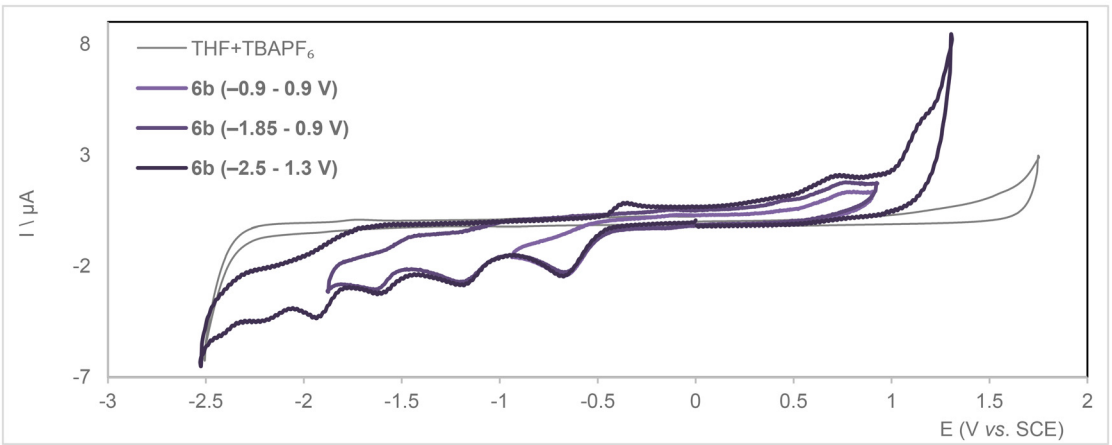

Fig. 7 Cyclic voltammograms for compound **6b** (bottom) ([C] = 1 mM) recorded over different voltage ranges under Ar in dry THF with 0.1 M TBA[PF_6] supporting electrolyte (ν = 0.2 V s^{-1}).

in which the bpp ligand is deprotonated. We managed to obtain these new complexes selectively in moderate to good isolated yields by adding 2 equiv. of an oxidant (Ag^+) to the reaction mixture. These were characterized by means of NMR, IR and UV-Vis spectroscopies, sc-XRD as well as circular and square-wave voltammetries for **4a**, **4b** and **5b**. UV-Vis spectra of the series, especially those of **4b** and **4c** and **5b** and **5c** that show well-defined absorptions in the near-UV that are not influenced by the nature of the phosphines, point to IL and MLCT being presumably the least energetic transitions. In CV, the complexes investigated have in common the irreversibility of their first reduction wave (occurring below −1.5 V *vs.* SCE), being probably ligand-centered, and the reversibility of their first oxidation wave (occurring above 0.5 V) that we assigned to the Mo^{3+}/Mo^{2+} couple. The deprotonated $\mathbf{L}^{\mathbf{tBu}}$ ligand in **5a–c** can be readily re-protonated with 2 equiv. of HOTf to afford the dicationic $[Mo(CO)_2(\mathbf{L}^{\mathbf{tBu}})(PMe_{3-n}Ph_n)_2][OTf]_2$ complexes, but the same reaction in the case of the $\mathbf{L}^{\mathbf{CF3}}$ series resulted in decomposition of intractable mixtures of compounds. This study provides further insights into the interaction of low-oxidation molybdenum with ligands that can potentially develop a non-innocent character. Our attempts with Mo(0) strongly suggest the non-innocence of the bpp platform, and the electrochemistry of Mo(II) complexes hints that an electron can be stored on the ligand, but at the cost of stability. Further engineering of low-valent Mo complexes is therefore needed to control and exploit the non-innocence of the surrounding bpp platform.

Experimental methods

General considerations

All reactions were performed in flame- or oven-dried glassware with rigorous exclusion of air and moisture, using Schlenk line techniques or Jacomex (argon and dinitrogen) glove boxes (O_2 < 1.0 ppm, H_2O < 1 ppm). All of the experiments were carried out under an argon atmosphere. Solvents used were pre-dried by passing through a Puresolv MD 7 solvent purification machine, degassed by freeze–pump–thaw cycles (except for acetonitrile degassed by bubbling argon inside the solvent), dried over molecular sieves and stored in an argon glove box. The deuterated solvent (purchased from Eurisotop) was degassed by freeze–pump–thaw cycles, dried over molecular sieves and stored in an argon glove box. ^{1}H, ^{13}C, ^{19}F and ^{31}P NMR spectra were recorded using NMR tubes equipped with J. Young valves on a Bruker Avance III 400 spectrometer. Chemical shifts are reported in parts per million (ppm) downfield from tetramethylsilane and are referenced to the most upfield residual solvent resonance as the internal standard in ^{1}H NMR (THF-d_8: δ reported = 1.72 ppm; CD_3CN: δ reported = 1.94 ppm). ^{19}F and ^{31}P NMR spectra were calibrated according to the IUPAC recommendation using a unified chemical shift scale based on the proton resonance of tetramethylsilane as the primary reference.[86] Data are reported as follows: chemical shift, multiplicity (b = broad, s = singlet, d = doublet, t = triplet, q = quartet, quint = quintet, m = multiplet), coupling constant (Hz), and integration. Infrared (IR) spectra were recorded in a dinitrogen glove box (O_2 < 1.0 ppm, H_2O < 1 ppm) on an Agilent Cary 630 FT-IR spectrophotometer equipped with ATR or transmission modules and are reported in wavenumbers (cm^{-1}) with (s), (m), and (w) indicating strong, medium, and weak absorption respectively. UV-Vis spectra were recorded on a PerkinElmer LAMBDA 950 UV/vis spectrophotometer equipped with a dual-beam setup. The UV cells (quartz cells equipped with airtight Teflon caps, 10 mm light path) were prepared under air with the solvent dried and degassed (as explained previously). Elemental analyses were performed on samples sealed in tin capsules under Ar or N_2 by the Analytical Service of the Laboratoire de Chimie de Coordination; the results are the average of two independent measurements.

Syntheses

The syntheses of complexes **1–3** have been done as reported in the literature from unpurified, commercially available chemicals and stored in a glove box.[71–74] Also, the syntheses of both ligands $\mathbf{L}^{\mathbf{CF3}}$ or $\mathbf{L}^{\mathbf{tBu}}$ have been done as reported in the literature.[42,87] For all the heptacoordinated complexes (**4a–c** and **5b–c**) except for **5a**, a common procedure was used for the syntheses.

4a–c: In a 25 mL vial, a solution containing $\mathbf{L}^{\mathbf{CF3}}$ (1.0 mmol, 1.0 equiv.) in 5 mL of THF is added under stirring to a solution of the metallic precursor (**1**/**2**/**3**, 1.0 mmol, 1.0 equiv.) solubilized in 5 mL of THF. Then, a solution of AgOAc (2.1 mmol, 2.1 equiv.) in 10 mL of THF is added dropwise over the course of 5 minutes. The solution is left under stirring at room temperature for 3 h, during which dark red/orange coloration appears. The crude product is filtered to separate metallic silver that precipitated, and the volatiles are removed under vacuum. The orange/brown oil recovered is washed two times with pentane (2 × 5 mL) and two times with diethyl ether (2 × 5 mL). The precipitate is separated from the solution by filtration with a filtrating cannula, to obtain **4a–c** as red solids in 40%, 69% and 70% yields, respectively.

4a: ^{1}H NMR (400 MHz, THF-d_8) δ 7.70 (t, J = 7.9 Hz, 1H), 7.28 (t, J = 7.5 Hz, 6H), 7.09 (t, J = 7.6 Hz, 12H), 6.99–6.92 (m, 13H overlapping), 6.36 (s, 2H); ^{31}P{^{1}H} NMR (162 MHz, THF-d_8) δ 37.75 (s, 2P); ^{19}F NMR (377 MHz, THF-d_8) δ −61.61; ^{13}C{^{1}H} NMR (101 MHz, THF-d_8) δ 267.12 (t, J = 18.2 Hz), 134.65 (d, J = 6.0 Hz), 130.98, 129.04 (t, J = 4.6 Hz), 117.00, 104.29; IR (ATR, solid): $\bar{\nu}$ 1944 cm^{-1} (s, C═O as); 1888 cm^{-1} (s, C═O *sym*); anal. calcd for $C_{51}H_{35}F_6MoN_5O_2P_2$; C 59.95, H 3.45, N 6.85; found C 59.63, H 3.34, N 6.94.

4b: ^{1}H NMR (400 MHz, THF-d_8) δ 7.45 (t, 1H), 7.21 (t, J = 7.4 Hz, 4H), 7.00 (t, 8H), 6.87 (d, J = 7.9 Hz, 2H), 6.74 (s, 2H), 6.68 (q, 8H), 1.63 (t, J = 3.5 Hz, 2H); ^{31}P{^{1}H} NMR (162 MHz, THF-d_8) δ 22.60 (s, 2P); ^{19}F NMR (377 MHz, THF-d_8) δ −61.55 (s, 6F); ^{13}C{^{1}H} NMR (101 MHz, THF-d_8) δ 267.48, 152.50, 150.80, 139.95, 132.70 (t, J = 5.5 Hz), 130.62, 129.08 (t, J = 4.6 Hz), 116.24, 104.31, 11.70; IR (ATR, solid): $\bar{\nu}$ 1948 cm^{-1} (s, C═O as);

1880 cm^{-1} (s, C═O *sym*); anal. calcd for $C_{41}H_{31}F_6MoN_5O_2P_2$: C 54.86, H 3.48, N 7.80 found C 53.93, H 3.53, N 7.50.

4c: ^{1}H NMR (400 MHz, THF-d_8) δ 7.53 (t, J = 7.8 Hz, 1H), 7.12 (t, J = 7.4 Hz, 2H), 7.04 (d, J = 7.8 Hz, 2H), 6.92 (t, J = 7.6 Hz, 4H), 6.87 (s, 2H), 6.52–6.42 (m, 4H), 1.23 (t, 12H); ^{31}P{H} NMR (162 MHz, THF-d_8) δ 9.64 (s, 2P); ^{19}F NMR (377 MHz, THF-d_8) δ −61.50 (s, 6F); ^{13}C{^{1}H} NMR (101 MHz, THF-d_8) δ 264.01, 151.02, 149.78, 138.34, 128.65 (t, J = 4.9 Hz), 128.40, 127.41 (t, J = 4.4 Hz), 114.46, 102.28, 10.90 (t, J = 13.1 Hz); IR (ATR, solid): $\bar{\nu}$ 1934 cm^{-1} (s, C═O as); 1873 (s, C═O *sym*); anal. calcd for $C_{41}H_{31}F_6MoN_5O_2P_2$: C 48.14, H 3.52, N 9.05 found C 48.79, H 3.77, N 8.53.

5a: In a 25 mL vial, a solution containing $\mathbf{L}^{t\mathbf{Bu}}$ (1.0 mmol, 1.0 equiv.) in 5 mL of THF is added under stirring to a solution of the metallic precursor (**1**, 1.0 mmol, 1.0 equiv.) solubilized in 5 mL of THF. Then, a solution of Ag_2O (2.1 mmol, 2.1 equiv.) in 10 mL of THF is added dropwise over the course of 5 minutes. The solution is left under stirring at room temperature for 20 h, during which dark red/orange coloration appears. The crude product is filtered to separate metallic silver that precipitated, and the volatiles are removed under vacuum. The orange/brown oil recovered is washed three times with cold (−40 °C) pentane (3 × 5 mL) and three times with cold (−40 °C) diethyl ether (3 × 5 mL). The precipitate is separated from the solution by filtration with a filtrating cannula, to obtain a red/brown solid in 51% yield. However, the calculated yield is not accurate because this compound could not be isolated in pure form. ^{1}H NMR (400 MHz, THF-d_8) δ 7.22 (t, J = 7.3 Hz, 1H), 7.05 (t overlapping, J = 7.5 Hz), 6.63 (d, J = 7.8 Hz, 2H), 5.91 (s, J = 0.8 Hz, 2H), 1.40 (s, 18H); ^{31}P{^{1}H} NMR (162 MHz, THF-d_8) δ 37.14 (s, 2P) free PPh_3 at δ −4.86 (s, 1P); ^{13}C{^{1}H} NMR (101 MHz, THF-d_8) δ 134.83, 134.63, 134.06 (t, J = 6.2 Hz), 130.27, 129.69 (d, J = 3.8 Hz), 129.44 (dd, J = 7.2, 2.7 Hz), 129.08 (q, J = 4.1 Hz), 114.52 (d, J = 4.3 Hz), 101.01, 31.93; IR (ATR, solid): $\bar{\nu}$ 1938 cm^{-1} (s, C═O as); 1886 (s, C═O *sym*).

5b and **5c**: In a 25 mL vial, a solution containing $\mathbf{L}^{t\mathbf{Bu}}$ (1.0 mmol, 1.0 equiv.) in 5 mL of THF is added under stirring to a solution of the metallic precursor (**2** or **3**, 1.0 mmol, 1.0 equiv.) solubilized in 5 mL of THF. Then, a solution of AgOAc (2.1 mmol, 2.1 equiv.) in 10 mL of THF is added dropwise over the course of 5 minutes. The solution is left under stirring at room temperature for 20 h, during which a dark red/orange coloration appears. The crude product is filtered to separate metallic silver that precipitated, and the solution is dried under vacuum. The orange/brown oil recovered is washed twice with pentane (2 × 5 mL) and twice with diethyl ether (2 × 5 mL). The precipitate is separated from the solution by filtration with a filtrating cannula, to obtain **5b** and **5c** as red solids in 44% and 50% yields, respectively.

5b: ^{1}H NMR (40 MHz, THF-d_8) δ 7.45 (t, 1H), 7.21 (t, J = 7.4 Hz, 4H), 7.00 (t, 8H), 6.87 (d, J = 7.9 Hz, 2H), 6.74 (s, 2H), 6.68 (q, 8H), 1.63 (t, J = 3.5 Hz, 2H); ^{31}P{^{1}H} NMR (162 MHz, THF-d_8) δ 22.60 (s, 2P); ^{19}F NMR (377 MHz, THF-d_8) δ −61.55 (s, 6F); ^{13}C{^{1}H} NMR (400 MHz, THF-d_8) δ 267.48, 152.50, 150.80, 139.95, 132.70 (t, J = 5.5 Hz), 130.62, 129.08 (t, J = 4.6 Hz), 116.24, 104.31, 11.70; IR (ATR, solid): $\bar{\nu}$ 1940 cm^{-1} (s, C═O as); 1879 (s, C═O *sym*); anal. calcd for $C_{47}H_{49}MoN_5O_2P_2$; C 64.60, H 5.65, N 5.65, found C 63.73, H 5.76, N 6.62.

5c: ^{1}H NMR (400 MHz, THF-d_8) δ 7.34 (t, 1H), 7.10 (t, J = 7.5, 5.9, 1.8, 0.9 Hz, 2H), 6.94 (t, J = 8.7, 7.6, 1.2 Hz, 4H), 6.79 (d, J = 7.8 Hz, 2H), 6.63 (dtt, J = 8.4, 5.0, 1.5 Hz, 4H), 6.43 (s, 2H), 1.36 (s, 19H), 1.12 (t, 12H); ^{31}P{^{1}H} NMR (162 MHz, THF-d_8) δ 11.11 (s, 2P); ^{13}C{^{1}H} NMR (101 MHz, THF) δ 266.93 (t, J = 17.2 Hz), 167.52, 130.91, 129.60, 129.16 (d, J = 5.3 Hz), 128.60 (t, J = 4.3 Hz), 113.38, 100.22, 31.77, 12.57 (t, J = 12.2 Hz); IR (ATR, solid): $\bar{\nu}$ 1946 cm^{-1} (s, C═O as); 1877 (s, C═O *sym*).

6a–c: A common synthetic protocol was used for these complexes as described below.

In a 50 mL Schlenk tube connected to a Schlenk line, HOTf (0.4 mmol, 2.0 equiv.) is added under stirring to a cold (273 K) solution of **1**/**2**/**3** (0.2 mmol, 1.0 equiv.) in 20 mL of THF. Then, the solution is left under stirring at room temperature for 4 h. The pale-yellow precipitate formed is filtered and dried under vacuum to afford complexes **6a–c** in 30%, 77% and 33% yields, respectively.

6a: ^{1}H NMR (400 MHz, CD_3CN) δ 11.69 (s, 2H), 7.94 (t, 0H), 7.49 (t, 6H), 7.45–7.36 (m, 2H), 7.29 (t, J = 7.8 Hz, 2H), 6.75 (q, J = 6.7, 6.3 Hz, 12H), 1.26 (s, 18H); ^{31}P{^{1}H} NMR (162 MHz, CD_3CN) δ 39.60; ^{19}F NMR (377 MHz, CD_3CN) δ −79.20; IR (ATR, solid): $\bar{\nu}$ 1953 cm^{-1} (s, C═O as); 1900 (s, C═O *sym*).

6b: ^{1}H NMR (400 MHz, CD_3CN) δ 12.09 (s, 2H), 7.94 (t, J = 7.9, 1.2 Hz, 1H), 7.50–7.38 (m, 6H), 7.20 (dt, J = 23.4, 7.6 Hz, 9H), 6.84–6.74 (m, 6H), 6.62–6.52 (m, 4H), 1.60 (t, J = 3.7 Hz, 6H), 1.42 (s, 18H); ^{31}P{^{1}H} NMR (162 MHz, CD_3CN) δ 23.16 (s, 2P); ^{19}F NMR (377 MHz, CD_3CN) δ −79.22 (s, 6F); ^{13}C{^{1}H} NMR (101 MHz, CD_3CN) δ 264.30 (t, J = 20.9 Hz), 165.26, 153.03, 148.17, 143.33, 132.77–132.13 (m), 130.26 (q, J = 5.4 Hz), 122.99, 118.32, 105.74, 32.98, 29.94, 11.81 (t, J = 14.8 Hz); IR (ATR, solid): $\bar{\nu}$ 1962 cm^{-1} (s, C═O as); 1908 (s, C═O *sym*); anal. calcd for $C_{49}H_{51}F_6MoN_5O_8P_2S_2$; C 50.13, H 4.38, N 5.97; found C 49.85, 4.39, H 5.98.

6c: ^{1}H NMR (400 MHz, CD_3CN) δ 12.02 (s, 2H), 7.97 (t, 1H), 7.49 (d, J = 8.0 Hz, 2H), 7.26 (t, 2H), 6.99 (t, J = 8.7, 7.5, 1.3 Hz, 4H), 6.78 (d, J = 2.0 Hz, 2H), 6.40–6.30 (m, 4H), 1.41 (s, 18H), 1.34 (t, J = 4.4 Hz, 12H); ^{31}P{^{1}H} NMR (162 MHz, CD_3CN) δ 8.31 (s, 2P); ^{19}F NMR (377 MHz, CD_3CN) δ −79.18 (s, 6F); ^{13}C{^{1}H} NMR (101 MHz, CD_3CN) δ 263.94 (t, J = 20.1 Hz), 164.30, 152.84, 148.38, 142.89, 131.27, 129.93 (t, J = 4.6 Hz), 129.56 (t, J = 4.6 Hz), 122.42, 118.32, 105.04, 29.91; IR (ATR, solid): $\bar{\nu}$ 1953 cm^{-1} (s, C═O as); 1887 (s, C═O *sym*).

Author contributions

A. E., L. E. B., L. P., R. P. and N. G. ran the experiments and analysed the data. A. S.-S. performed the electrochemical measurements. L. V. performed the X-ray diffraction studies and solved the structures. A. S. and M. G. conceived the project and managed it. A. S., M. G., R. S. and N. F. acquired funding. A. S., M. G., R. S., N. F. and J.-B. S. supervised the work. A. S. wrote the manuscript. A. E., L. E. B. and

A. S. compiled the ESI.† All co-authors were involved in manuscript and ESI† proof-reading.

Data availability

The datasets are available on request from the authors. Results of data treatment (NMR, infrared and UV-Vis spectra, crystallographic details, cyclic and square wave voltammograms) have been compiled in a .pdf file freely available as part of the ESI.† X-ray diffraction data have been deposited on the Cambridge Crystallographic Data Centre (CCDC) under the deposition numbers 2403147–2403152.†

Conflicts of interest

The authors declare no conflicts of interest.

Acknowledgements

A. E. and A. S. acknowledge the Région Occitanie and Pôle RHyO for funding (grant CataLOHC). L. E. B., R. S., N. F. and A. S. have received funding from a CNRS "International Research Project". All authors thank their respective institutions for providing access to facilities.

References

1 *Pincer Compounds*, ed. D. Morales-Morales, Elsevier, 2018.
2 E. Peris and R. H. Crabtree, *Chem. Soc. Rev.*, 2018, **47**, 1959–1968.
3 M. A. W. Lawrence, K.-A. Green, P. N. Nelson and S. C. Lorraine, *Polyhedron*, 2018, **143**, 11–27.
4 H. Valdés, M. A. García-Eleno, D. Canseco-Gonzalez and D. Morales-Morales, *ChemCatChem*, 2018, **10**, 3136–3172.
5 *Organometallic Pincer Chemistry*, ed. G. van Koten and D. Milstein, Springer, 2012.
6 G. van Koten, *Pure Appl. Chem.*, 1989, **61**, 1681–1694.
7 A. Kasera, J. P. Biswas, A. Ali Alshehri, S. Ahmed Al-Thabaiti, M. Mokhtar and D. Maiti, *Coord. Chem. Rev.*, 2023, **475**, 214915.
8 K. K. Manar, J. Cheng, Y. Yang, X. Yang and P. Ren, *ChemCatChem*, 2023, **15**, e202300004.
9 *Metal-Ligand Co-operativity: Catalysis and the Pincer-Metal Platform*, ed. G. van Koten, K. Kirchner and M.-E. Moret, Springer International Publishing, 2021.
10 L. Alig, M. Fritz and S. Schneider, *Chem. Rev.*, 2019, **119**, 2681–2751.
11 T. Zell and D. Milstein, *Acc. Chem. Res.*, 2015, **48**, 1979–1994.
12 C. Gunanathan and D. Milstein, *Chem. Rev.*, 2014, **114**, 12024–12087.
13 J. I. van der Vlugt and J. N. H. Reek, *Angew. Chem., Int. Ed.*, 2009, **48**, 8832–8846.
14 M. A. Halcrow, *Coord. Chem. Rev.*, 2005, **249**, 2880–2908.
15 T. Buchen, P. Guetlich and H. A. Goodwin, *Inorg. Chem.*, 1994, **33**, 4573–4576.
16 L. A. Barrios, C. Bartual-Murgui, E. Peyrecave-Lleixà, B. Le Guennic, S. J. Teat, O. Roubeau and G. Aromí, *Inorg. Chem.*, 2016, **55**, 4110–4116.
17 V. Jornet-Mollá, Y. Duan, C. Giménez-Saiz, Y.-Y. Tang, P.-F. Li, F. M. Romero and R.-G. Xiong, *Angew. Chem., Int. Ed.*, 2017, **56**, 14052–14056.
18 A. Djemel, O. Stefanczyk, M. Marchivie, E. Trzop, E. Collet, C. Desplanches, R. Delimi and G. Chastanet, *Chem. – Eur. J.*, 2018, **24**, 14760–14767.
19 S. P. Vallone, A. N. Tantillo, A. M. dos Santos, J. J. Molaison, R. Kulmaczewski, A. Chapoy, P. Ahmadi, M. A. Halcrow and K. G. Sandeman, *Adv. Mater.*, 2019, **31**, 1807334.
20 M. A. Halcrow, I. Capel Berdiell, C. M. Pask and R. Kulmaczewski, *Inorg. Chem.*, 2019, **58**, 9811–9821.
21 C.-Y. Kuei, S.-H. Liu, P.-T. Chou, G.-H. Lee and Y. Chi, *Dalton Trans.*, 2016, **45**, 15364–15373.
22 J. Yan, M. Song, D.-Y. Zhou, S.-M. Yiu, L.-S. Liao, Y. Chi and M. Xie, *Organometallics*, 2023, **42**, 2070–2078.
23 D. A. Bardwell, J. C. Jeffery, P. L. Jones, J. A. McCleverty, E. Psillakis, Z. Reeves and M. D. Ward, *J. Chem. Soc., Dalton Trans.*, 1997, 2079–2086.
24 Y.-W. Yip, H. Wen, W.-T. Wong, P. A. Tanner and K.-L. Wong, *Inorg. Chem.*, 2012, **51**, 7013–7015.
25 A. Galstyan, A. R. Naziruddin, C. Cebrián, A. Iordache, C. G. Daniliuc, L. De Cola and C. A. Strassert, *Eur. J. Inorg. Chem.*, 2015, **2015**, 5822–5831.
26 C.-C. Chou, K.-L. Wu, Y. Chi, W.-P. Hu, S. J. Yu, G.-H. Lee, C.-L. Lin and P.-T. Chou, *Angew. Chem., Int. Ed.*, 2011, **50**, 2054–2058.
27 T. Kono, N. Masaki, M. Nishikawa, R. Tamura, H. Matsuzaki, M. Kimura and S. Mori, *ACS Appl. Mater. Interfaces*, 2016, **8**, 16677–16683.
28 P. Delcanale, A. Galstyan, C. G. Daniliuc, H. E. Grecco, S. Abbruzzetti, A. Faust, C. Viappiani and C. A. Strassert, *ACS Appl. Mater. Interfaces*, 2018, **10**, 24361–24369.
29 C. Adam, B. B. Beele, A. Geist, U. Müllich, P. Kaden and P. J. Panak, *Chem. Sci.*, 2015, **6**, 1548–1561.
30 J. Stracke, P. Weßling, T. Sittel, C. Adam, F. Rominger, A. Geist and P. J. Panak, *Inorg. Chem.*, 2024, **63**, 13214–13222.
31 S. Radisavljević, I. Bratsos, A. Scheurer, J. Korzekwa, R. Masnikosa, A. Tot, N. Gligorijević, S. Radulović and A. R. Simović, *Dalton Trans.*, 2018, **47**, 13696–13712.
32 D. Ćoćić, S. Jovanović, S. Radisavljević, J. Korzekwa, A. Scheurer, R. Puchta, D. Baskić, D. Todorović, S. Popović, S. Matić and B. Petrović, *J. Inorg. Biochem.*, 2018, **189**, 91–102.
33 M. M. Milutinović, J. V. Bogojeski, O. Klisurić, A. Scheurer, S. K. C. Elmroth and Ž. D. Bugarčić, *Dalton Trans.*, 2016, **45**, 15481–15491.
34 N. S. Labrum, C.-H. Chen and K. G. Caulton, *Chem. – Eur. J.*, 2019, **25**, 7935–7940.

35 N. S. Labrum, A. C. Cabelof and K. G. Caulton, *Chem. – Eur. J.*, 2020, **26**, 13915–13926.
36 B. J. Cook, C.-H. Chen and K. G. Caulton, *Chem. – Eur. J.*, 2018, **24**, 5962–5966.
37 J. J. Kiernicki, M. Zeller and N. K. Szymczak, *Inorg. Chem.*, 2020, **59**, 9279–9286.
38 J. L. Kuo and K. I. Goldberg, *J. Am. Chem. Soc.*, 2020, **142**, 21439–21449.
39 K. Umehara, S. Kuwata and T. Ikariya, *J. Am. Chem. Soc.*, 2013, **135**, 6754–6757.
40 J. J. Kiernicki, M. Zeller and N. K. Szymczak, *J. Am. Chem. Soc.*, 2017, **139**, 18194–18197.
41 B. J. Cook, A. V. Polezhaev, C.-H. Chen, M. Pink and K. G. Caulton, *Inorg. Chim. Acta*, 2018, **483**, 510–515.
42 A. Yoshinari, A. Tazawa, S. Kuwata and T. Ikariya, *Chem. – Asian J.*, 2012, **7**, 1417–1425.
43 T. J. Sherbow, J. C. Fettinger and L. A. Berben, *Inorg. Chem.*, 2017, **56**, 8651–8660.
44 Y. Nakahara, T. Toda and S. Kuwata, *Polyhedron*, 2018, **143**, 105–110.
45 P. Weingart and W. R. Thiel, *ChemCatChem*, 2018, **10**, 4844–4848.
46 Y. Nakahara, T. Toda, A. Matsunami, Y. Kayaki and S. Kuwata, *Chem. – Asian J.*, 2018, **13**, 73–80.
47 C. Wu, B. Liu, X. Geng, Z. Zhang, S. Liu and Q. Hu, *Polyhedron*, 2019, **158**, 334–341.
48 Y. Chen, T. Cui, H. Chen, X. li Zheng, H. Fu and R. Li, *Dalton Trans.*, 2023, **52**, 12368–12377.
49 A. Simonneau, R. Turrel, L. Vendier and M. Etienne, *Angew. Chem., Int. Ed.*, 2017, **56**, 12268–12272.
50 A. Coffinet, D. Specklin, L. Vendier, M. Etienne and A. Simonneau, *Chem. – Eur. J.*, 2019, **25**, 14300–14303.
51 A. Bouammali, C. Bijani, L. Vendier, M. Etienne and A. Simonneau, *Eur. J. Inorg. Chem.*, 2020, **2020**, 1423–1427.
52 A. Coffinet, D. Zhang, L. Vendier, S. Bontemps and A. Simonneau, *Dalton Trans.*, 2021, **50**, 5582–5589.
53 D. Specklin, A. Coffinet, L. Vendier, I. del Rosal, C. Dinoi and A. Simonneau, *Inorg. Chem.*, 2021, **60**, 5545–5562.
54 A. Bouammali, A. Coffinet, L. Vendier and A. Simonneau, *Dalton Trans.*, 2022, **51**, 10697–10701.
55 D. Specklin, M.-C. Boegli, A. Coffinet, L. Escomel, L. Vendier, M. Grellier and A. Simonneau, *Chem. Sci.*, 2023, **14**, 14262–14270.
56 N. Queyriaux, N. Durvin, D. Leon, M.-C. Boegli, L. Vendier and A. Simonneau, *Eur. J. Inorg. Chem.*, 2023, **26**, e202300426.
57 Q. Le Dé, F. Orbay, L. Vendier and A. Simonneau, *J. Organomet. Chem.*, 2023, **986**, 122604.
58 W. R. Thiel and J. Eppinger, *Chem. – Eur. J.*, 1997, **3**, 696–705.
59 K. Arashiba, Y. Miyake and Y. Nishibayashi, *Nat. Chem.*, 2011, **3**, 120–125.
60 S. Kuriyama, K. Arashiba, K. Nakajima, H. Tanaka, N. Kamaru, K. Yoshizawa and Y. Nishibayashi, *J. Am. Chem. Soc.*, 2014, **136**, 9719–9731.
61 S. Chakraborty and H. Berke, *ACS Catal.*, 2014, **4**, 2191–2194.
62 Y. Zhang, P. G. Williard and W. H. Bernskoetter, *Organometallics*, 2016, **35**, 860–865.
63 T. Leischner, A. Spannenberg, K. Junge and M. Beller, *Organometallics*, 2018, **37**, 4402–4408.
64 T. Leischner, L. A. Suarez, A. Spannenberg, K. Junge, A. Nova and M. Beller, *Chem. Sci.*, 2019, **10**, 10566–10576.
65 T. Leischner, A. Spannenberg, K. Junge and M. Beller, *ChemCatChem*, 2020, **12**, 4543–4549.
66 T. Itabashi, K. Arashiba, A. Egi, H. Tanaka, K. Sugiyama, S. Suginome, S. Kuriyama, K. Yoshizawa and Y. Nishibayashi, *Nat. Commun.*, 2022, **13**, 6161.
67 N. F. Both, A. Spannenberg, K. Junge and M. Beller, *Organometallics*, 2022, **41**, 1797–1805.
68 P. Viereck, G. Hierlmeier, P. Tosatti, T. P. Pabst, K. Puentener and P. J. Chirik, *J. Am. Chem. Soc.*, 2022, **144**, 11203–11214.
69 A. F. Ibrahim, P. Garrido-Barros and J. C. Peters, *ACS Catal.*, 2023, **13**, 72–78.
70 N. F. Both, J. Thaens, A. Spannenberg, H. Jiao, K. Junge and M. Beller, *ACS Catal.*, 2024, **14**, 4082–4092.
71 F. Hohmann and H. T. Dieck, *J. Organomet. Chem.*, 1975, **85**, 47–71.
72 F. Hohmann, *J. Organomet. Chem.*, 1977, **137**, 315–328.
73 F. Hohmann, H. tom Dieck, C. Krüger and Y.-H. Tsay, *J. Organomet. Chem.*, 1979, **171**, 353–364.
74 B. J. Brisdon, D. A. Edwards and K. E. Paddick, *Transition Met. Chem.*, 1981, **6**, 83–86.
75 R. Hoffmann, B. F. Beier, E. L. Muetterties and A. R. Rossi, *Inorg. Chem.*, 1977, **16**, 511–522.
76 B. J. Cook, M. Pink, K. Pal and K. G. Caulton, *Inorg. Chem.*, 2018, **57**, 6176–6185.
77 N. S. Labrum, G. M. Curtin, E. Jakubikova and K. G. Caulton, *Chem. – Eur. J.*, 2020, **26**, 9547–9555.
78 C. A. Tolman, *Chem. Rev.*, 1977, **77**, 313–348.
79 F.-Q. Bai, X. Zhou, T. Liu, G.-J. Zhao, J.-P. Zhang and H.-X. Zhang, *Int. J. Quantum Chem.*, 2009, **109**, 308–319.
80 Y. Chi, B. Tong and P.-T. Chou, *Coord. Chem. Rev.*, 2014, **281**, 1–25.
81 M. Wrighton, *Chem. Rev.*, 1974, **74**, 401–430.
82 W. A. Fordyce and G. A. Crosby, *Inorg. Chem.*, 1982, **21**, 1455–1461.
83 P. D. Harvey, W. P. Schaefer and H. B. Gray, *Inorg. Chem.*, 1988, **27**, 1101–1104.
84 H. Tominaga, K. Sakai and T. Tsubomura, *J. Chem. Soc., Chem. Commun.*, 1995, 2273–2274.
85 H. Kunkely and A. Vogler, *Inorg. Chem. Commun.*, 2000, **3**, 143–144.
86 R. K. Harris, E. D. Becker, S. M. Cabral de Menezes, R. Goodfellow and P. Granger, *Pure Appl. Chem.*, 2001, **73**, 1795–1818.
87 E. F. Khmara, D. L. Chizhov, A. A. Sidorov, G. G. Aleksandrov, P. A. Slepukhin, M. A. Kiskin, K. L. Tokarev, V. I. Filyakova, G. L. Rusinov, I. V. Smolyaninov, A. S. Bogomyakov, D. V. Starichenko, Yu. N. Shvachko, A. V. Korolev, I. L. Eremenko and V. N. Charushin, *Russ. Chem. Bull.*, 2012, **61**, 313–325.

